CURVELET DENOISING FOR PRECONDITIONING OF 2D POSTSTACK SEISMIC DATA INVERSION

V. M. Gomes, H. B. Santos, J. Schleicher, A. Novais, and M. A. C. Santos

email: *victormg@id.uff.br, hbuenos@gmail.com, js@ime.unicamp.br*
keywords: *Curvelet denoising, seismic pre-conditioning, poststack inversion*

ABSTRACT

Seismic inversion methods are highly sensitive to noise present in the data set. Most applications today attempt alternatives to achieve an amplification of the real signal, which corresponds to the subsurface structures, over the noise. The need to enhance the signal-to-noise ratio (SNR) motivated researchers do develop increasingly sophisticated denoising methods and combine them into other techniques. While some methodologies operate on a single scale, the curvelet transform established itself as multi-scale transform useful to decompose the seismic signals into multi-resolution elements. In this study, we evaluate the benefits of curvelet denoising as a preconditioning method for poststack seismic data in a 2D acoustic inversion processing using a Bayesian framework. Our tests on the Marmousi model and a real data set from a Brazilian offshore Basin have shown that the curvelet thresholding method can be successfully applied for random-noise elimination. Even the use of a hard global threshold led to improvements in the deepest parts. However, we observed a decrease of the SNR in the presence of soft rocks with pronounced absorption as they are typical in the shallowest regions. Future work will have to show whether alternatives that ensure a more robust way of selecting the coefficients can take into account the wavelength change with depth.

INTRODUCTION

The aim of seismic inversion methods is to provide a subsurface model which is coherent with the recorded seismic data. However, field-data applications often suffer from noise influence. The presence of noise brings instability to the inverse problem and makes it hard to estimate a reliable acoustic-impedance model, harming not only the wavelet recovery, but also the impedance estimate itself.

In the majority of denoising applications, we face the challenge of restoring the signal energy at high frequency without degrading the signal-to-noise ratio (SNR). This has motivated researchers to investigate sophisticated denoising techniques like localised slant stack (McMechan, 1983), T-X prediction filtering (Abma and Claerbout, 1995), and the sparse transform-based method (Yuan et al., 2015) for random-noise attenuation. Other techniques include the wavelet transform (Shan et al., 2009), which is able to detect local features in the time-frequency domain, and the S-transform adopted by (Parolai, 2009).

Candès and Donoho (2000) proposed the curvelet transform, a new multi-scale transform that can be used to decompose the seismic signals into multi-resolution elements. Moreover, the curvelets act in both the space-frequency domain and the angular orientation (Mallat, 1999). The features of curvelet decomposition proved itself as an adequate tool for application in many steps of seismic data processing (Ma and Plonka, 2010). Some applications include random-noise suppression by the combination of the thresholding method with a nonuniformly sampled curvelet transform (Hennenfent and Herrmann, 2006; Hennenfent et al., 2010), a curvelet-based noise attenuation method to treat 3D seismic data (Neelamani et al., 2008), the application of the curvelet denoising method to 2D and 3D seismic data (Górszczyk et al., 2014), multiple attenuation (Herrmann and Hennenfent, 2008), and migration (Chauris and Nguyen, 2008).

In this paper, we evaluate curvelet denoising as a preconditioning technique for acoustic inversion of poststack seismic data. We investigate its performance in noise suppression to a limit where visual and numerical artifacts become significantly dangerous to the data. Furthermore, because well-conditioned data ensure faster convergence, we study alternatives to achieve better results from the inversion of data with a significant amount of noise. For our evaluation, we choose two examples: the synthetic Marmousi model (Versteeg, 1994) and a real dataset from the Marimba oil field in the Campos Brazilian offshore Basin. Both analyses provide encouraging results.

THEORETICAL BACKGROUND

Curvelet Denoising for Seismic Data

Seismic data is composed of reflections with considerable continuity across volume sections. These reflections can be seen as geometric features composed mostly of line (2D) and surface (3D) singularities. In denoising, the data are usually transformed to some sparse domain, where coefficients associated with noise can be filtered out. For seismic purposes, such a transformation must assure that the mentioned singularities are precisely reconstructed after coefficient filtering. A well know sparsity-promoting transform is the Wavelet Transform (WT). However, even though it performs well for objects with point-like discontinuities by using isotropic elements, in 2D it fails for events with curve-like singularities. To overcome this WT drawback, Ma and Plonka (2010) proposed to use the Curvelet Transform (CT) with high directional sensitivity and anisotropic elements.

CT was first presented in Candès and Donoho (2000). Drawbacks in its discretization algorithm led to development of the second-generation Discrete Curvelet Transform (DCT) of Candès and Donoho (2003). This transform is a tight-frame capable of a near-optimal sparse representation of objects with discontinuities along smooth curve-like features by a series expansion using needle-shaped elements.

Using indices j for scale, k for rotation and $\boldsymbol{l}$ = (l_1,l_2)$\in \mathbb{Z}^2$ for translation, curvelets can be defined as a function of spatial position $\mathbf{x} = (x_1, x_2)$ in a continuous $\mathbb{R}^2$ space by

$$\zeta_{j,k,\boldsymbol{l}}(x) = \zeta_j(R_{\theta_{j,k}}(x - x_{\boldsymbol{l}}^{(j,k)})), \tag{1}$$

where $R_{\theta_{j,k}}$ is the rotation matrix for rotation angle $\theta_{j,k}$=$2\pi k \cdot 2^{-\lfloor j/2 \rfloor}$ with $k \in \mathbb{N}_0$, and each spatial position $x_{\boldsymbol{l}}^{(j,k)}$ is defined as $R_{\theta_{j,k}}^{-1}(l_1 2^{-j}, l_2 2^{-j/2})$. Therefore curvelets are obtained through anisotropic dilations, rotations and translations of a mother waveform ζ and the CT coefficients are the inner product of these curvelets and the data being analysed.

Curvelets have compact support in the frequency domain and each can be mapped to a localised polar wedge obeying the anisotropy scaling relation: length $\propto$ width^2. These wedges are functions of a pair of windows called $W(\rho)$ and $V(a)$, usually referred as radial and angular, through the relation

$$U_j(\rho, \theta) = 2^{-3j/4} W(2^{-j}\rho) V(\frac{2^{-\lfloor j/2 \rfloor}\theta}{2\pi}), \tag{2}$$

with $\rho \in (1/2, 2)$ and $a \in [-1, 1]$. Here, ρ and θ denote polar coordinates in the frequency domain. Window $W(\rho)$ partitions the frequency domain into ring-shaped regions and $V(a)$ divides it into wedges, as exemplified in Figure 1. It must be pointed out that the coarsest level CT element is an isotropic one much like WT elements.

Candès et al. (2006) discussed two approaches to implement the second-generation CT, one via unequally spaced fast Fourier transform and one via wrapping of specific Fourier samples. Here, we adopted the latter procedure, because it represents a tight frame and is computationally faster than the former.

Denoising assumes additive noise and uses a method like the one of Starck et al. (2002). It calculates an approximate value for the noise amplitude at each scale (standard deviation $\tilde{\sigma}_k$) using Monte Carlo simulations. Then, the filtered coefficients $\hat{y}_k$ are estimated from their noise-corrupted versions y_k by means of the hard-thresholding rule

$$\begin{cases} \hat{y}_k = y_k & \text{if } |y_k|/\sigma \geq \tau\tilde{\sigma}_k \\ \hat{y}_k = 0 & \text{if } |y_k|/\sigma < \tau\tilde{\sigma}_k \end{cases}, \tag{3}$$

where τ represents a relative threshold value and σ is an estimate of the noise level.

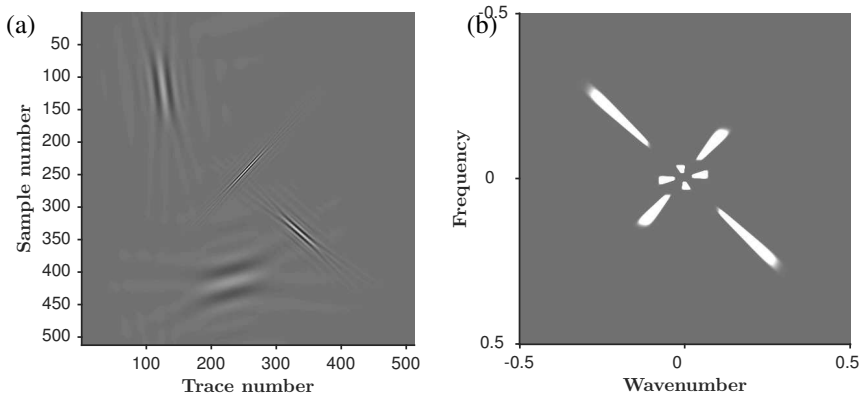

Figure 1: Four curvelets with different scale and angles represented in the (a) spatial and (b) frequency-wavenumber domain.

Poststack Acoustic Seismic Inversion

Seismic inversion methods can be separated into two main groups: prestack inversion including full-waveform inversion (FWI), and poststack inversion including the acoustic approach employed here. Despite depending on various assumptions that need to be satisfied for its validity, poststack techniques remain until today the standard tool for quantitative seismic interpretation.

An important problem for seismic inversion is the absence of low-frequency information in the seismic data due to the limited bandwidth. Pursuing a good initial model as an *a priori* constraint is a reasonable workaround to this barrier. Moreover, solving the inversion for a sparse spike-like reflectivity is an elegant mathematical solution to increase the bandwidth. Sparsity in ensured through regularisation using some sparse norm (e.g. L1, Huber, Cauchy).

Using a Bayesian framework, both sparsity ensuring regularisation norms and constraint dependence can be introduced in the objective function. For example, a blocky impedance model can be found, according to Ulrych and Sacchi (2005), from the minimisation of

$$J = \kappa|r|_{L1} + \frac{1}{2}\|\frac{1}{\sigma}(\mathbf{W}r - s)\|^2 + \frac{1}{2}\|\mathbf{N}^{-1}(\mathbf{C}r - B)\|^2\,, \tag{4}$$

where the first term is the sparsity norm, the second term is responsible for minimising the misfit between observed (real) and calculated data and the last constrains the model using the *a priori* information. Here, κ is a hyperparameter that ponders sparsity in the estimated reflectivity, r is the reflectivity, σ is an estimate of the noise level, $\mathbf{W}$ is the convolution matrix associated with the wavelet, s is the observed seismogram, $\mathbf{C}$ an integration operator or summation matrix, and B is the natural logarithm of the normalized impedance or double the cumulative sum of reflectivity. The term $\mathbf{N}$ is the diagonal matrix with $N_{k,k} = \lambda_k$, where λ is a vector of uncertainties of the *a priori* information. Thus, $\mathbf{N}$ is responsible for constraining the solution.

Ulrych and Sacchi (2005) discuss four sparsity norms, being Lp, Cauchy, Huber and Sech, but do not conclude which is the best. For that reason, we adopt Lp (with $p = 1$) norm, because it is easy to implement. A more thorough study would have to be performed in order to define the norm with the best performance in seismic inversion.

At last, it must be stressed that the choice of both κ and σ as well as construction of the initial model are probably the most important steps in the inversion process. They thus need much attention as they will define convergence to the global minimum of the objective function.

NUMERICAL EVALUATIONS

To evaluate the seismic data conditioning (here particularly denoising) using the curvelet transform and its impact on seismic inversion, we tested the procedure on both synthetic and real data.

Synthetics are based on the well-known acoustic Marmousi model shown in Figure 2. It was created in 1988 by the French Petroleum Institute based on a geological profile of the Kwanza basin in

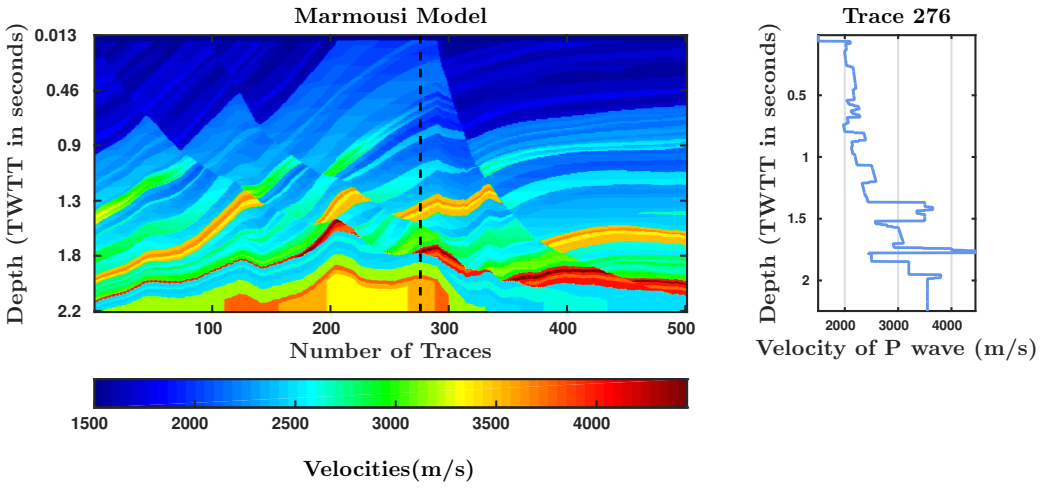

Figure 2: Marmousi P-velocity model and its 276th trace.

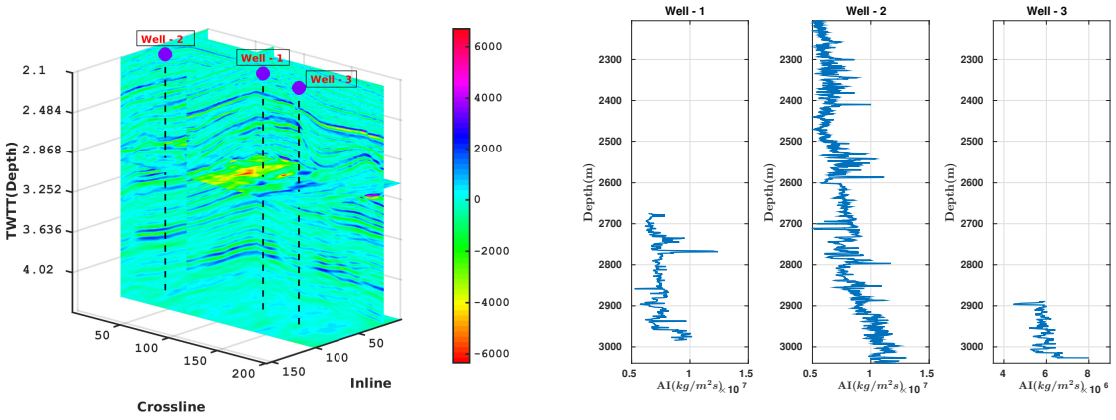

Figure 3: Real data: (a) Seismic volume with logs inside it and (b) the acoustic impedance logs for the wells.

North Quenguela (Versteeg, 1994). Its complex geological structure established it as, possibly, the most widespread model for performance analysis of seismic inversion and imaging algorithms, which is why we used this model.

The real data set is a section of a seismic volume from the Marimba oil field in the Campos Brazilian offshore Basin (see Figure 3). Additional information from three wells inside the volume was used to build the low-frequency model.

To generate the synthetic data, we used the convolutional model (initially described by Robinson, 1954), considering a Ricker wavelet with a central frequency of 20 Hertz. Modelling can be viewed as an approximation to an ideal zero-offset acquisition, where the wavelet is an idealisation of a waveform that could account both for the one created by the source and all the wavefield propagation phenomena changing it along time (i.e. dispersive effects). The convolutional model is the most adopted method to simulate post-stack seismic data. It depends on the assumptions that (1) the earth reflectivity is a random process and (2) the wavelet has minimum phase.

Our curvelet-filtering analysis used the method of Starck et al. (2002), described above. To understand how far curvelet denoising can work, we tested the method not only with the commonly used white Gaussian noise, but also using coloured noise (here white Gaussian noise band-limited to the data frequency

band), which has a higher influence on the low-frequency band in the inversion. Even though coloured noise is frequently present in seismic data, it is not usually studied in denoising research. However, because it affects the frequency band where inversion methods are most sensitive (the low-frequency part), it is paramount that denoising techniques are able to treat it. Our tests used four different values of the standard deviation (σ = 10e-3, 20e-3, 30e-3, and 50e-3). However, we considered only the first three values in the synthetic case. We adaptively chose threshold values with respect to the noise level, selecting from the values of $\tau = 5, 7.5, 10$, and 12 times σ.

The seismic-data inversion used a Bayesian acoustic poststack approach with an initial noise estimate of 5e-2 in for the synthetic data and 5e-4 for the real data. Seeking a better understanding of the wavelet inversion, we analysed both statistical and deterministic wavelets, because both can be used in inversion. The latter procedure is standard and has been shown to perform better for well-tying (de Macedo et al., 2017), a conclusion that can be extended to poststack inversion.

As a reference model for the real data, we used the result from inverting the same dataset with the Hampson-Russell software of CGG-Veritas. This choice was motivated by the fact that this is a standardly employed software for poststack acoustic-inversion purposes, providing plenty of tools to ensure that the inversion creates a good impedance model.

To measure the performance of the denoising and inversion methods, we used the peak signal-to-noise ratio (PSNR) and the L2-norm of the difference. PSNR is a standard measure in the research areas of signal denoising and compression, quantifying the presence of noise over signal. It is defined as

$$PSNR = 20 \log_{10} \left(\frac{MSV}{\sqrt{MSE}} \right) , \tag{5}$$

where MSV denotes the maximum signal value and MSE stands for the mean squared error between the original signal and its noisy version.

In any noise analysis, it is important to evaluate whether the modelled noise is representative for real situations or not. In the conditioning sense for poststack inversion, the data have already been preprocessed. Therefore, the noise is supposedly uncorrelated such that random-noise distributions as adopted here can be considered fair approximations.

Synthetic data - Marmousi model

White Gaussian noise. Our first test used white Gaussian noise on synthetic data from the Marmousi model. Filtering and inversion results for this case are summarised in Table 1. The first column shows the threshold value used in a certain experiment. The second column is divided into two parts, one showing the PSNR value after denoising and the other its change (increase positive, decrease negative) as compared to the noisy data. The third column exhibits the norm of the inversion error.

Figure 4 depicts the denoising results for the threshold value of $\tau = 7.5\sigma$. These figures can be considered representative because they contain the main features associated with the denoising analysis.

The main conclusion that can be drawn from these results is that the higher the threshold the smaller is the PSNR value. This behaviour can be related to the fact that filtering out more coefficients will possibly affect the ones associated with the most prominent reflections and certainly localised high-amplitude anomalies, reducing the maximum signal value and thus the PSNR. This filtering of information other than noise can be seen by the severe attenuation, particularly of the shallower reflections in Figure 4.

Looking at the zoom of trace 76 in Figure 4, we see two spikes. These are characteristic of wavelet transform thresholding known to create spike-like artifacts. Here, we employed them (using the Morlet wavelet) for the highest decomposition level in order to ensure that point-like features, which are unlikely to represent subsurface geology, are filtered out. Moreover, we recognize on both traces the diminishing amplitudes with increasing noise level as an effect of the increasing threshold.

Another effect of curvelet thresholding that must be discussed are the linear events, not physically consistent, that appear in the sections crossing the actual reflections. These events are the consequence of weak amplitude curvelets that emerge after inverse curvelet transformation. They can be easily removed by directional control (i.e. filtering curvelets by dip) as shown in Wang et al. (2010).

In general, our results show that this kind of inversion procedure can handle noise sufficiently well through regularisation, as long as a good estimate of σ is available.

	Threshold (X σ)	PSNR value(dB)	PSNR change	Error
Noise		**10e-3**		
	5	34.1338	+3.7765	0.1178
	7.5	32.8061	+2.4381	0.0868
	10	31.2612	+0.8935	0.0601
	12	30.3082	-0.0607	0.0282
Noise		**20e-3**		
	5	29.8906	+5.5478	0.1904
	7.5	29.0393	+4.6888	0.0612
	10	27.7386	+3.3826	0.0299
	12	26.8767	+2.5392	0.0251
Noise		**30e-3**		
	5	27.6170	+6.7812	0.2325
	7.5	27.0976	+6.2632	0.0419
	10	25.8594	+5.0306	0.0298
	12	25.0053	+4.1914	0.0346

Table 1: Results from white Gaussian noise tests in the Marmousi section.

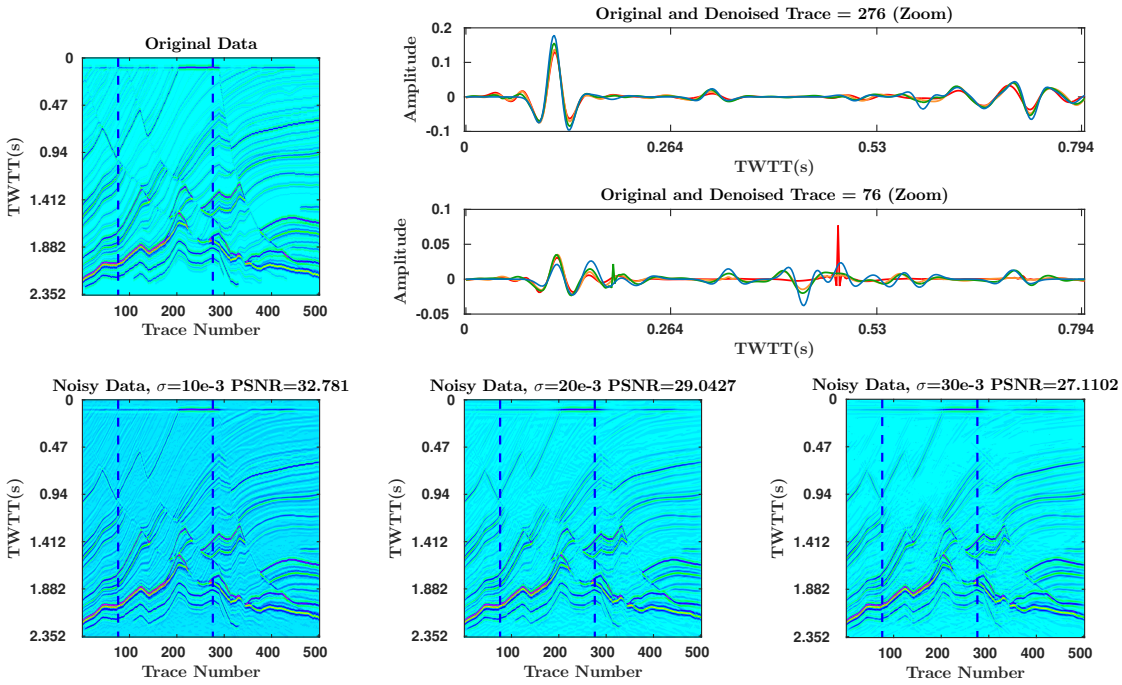

Figure 4: Denoising results considering three noise levels and a threshold of 7.5 times the noise level. In graphs, blue is the original trace and red, orange and green correspond to noise from higher to lower level, respectively.

From Table1, we see that the root-mean-square (rms) errors after curvelet denoising are considerably smaller than without filtering. This suggests it does a good job in removing the noise. Moreover, the error decays inversely to the thresholding value and the bigger the threshold the smaller are the number of low amplitude oscillations in the seismogram. Hence the inversion algorithm will have less trouble converging to a solution. However, in spite of the reduction of the rms error, impedance contrasts may be missed by the inversion and the estimated model may differ considerably from the real one, because filtering may reduce

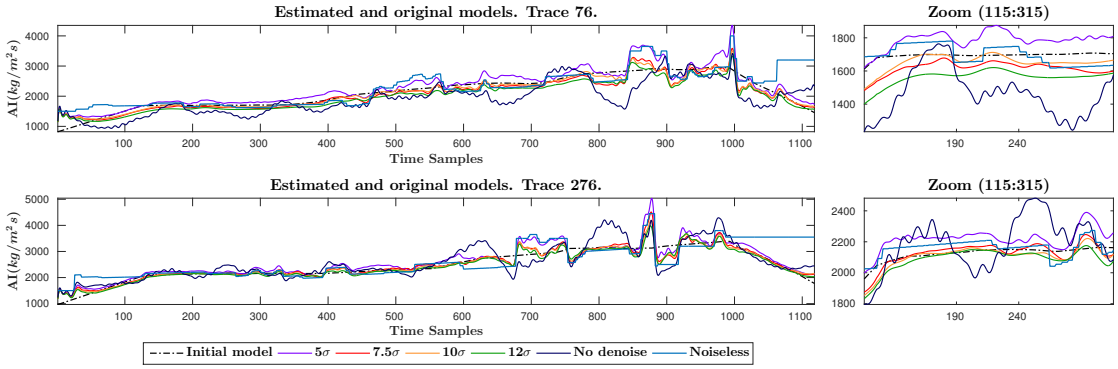

Figure 5: Inversion results for traces 76 and 276 after curvelet filtering the image polluted with a white Gaussian noise of $\sigma = 20\text{e-}3$. All thresholds are shown.

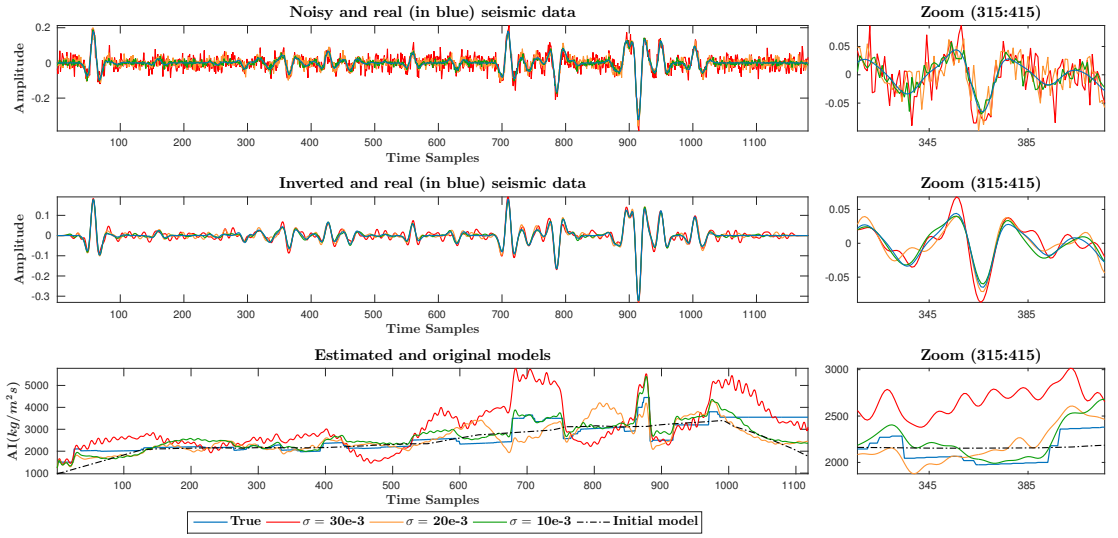

Figure 6: Inversion of trace 276 from seismic section with no filtering considering σ =10e-3 (green), 20e-3 (yellow) and 30e-3 (red) white Gaussian noises.

or even remove significant reflections.

The results from inverting traces 76 and 276 corrupted with a noise of $\sigma = 20\text{e-}3$ are shown in Figure 5. The results for this case are representative of the other noise levels. From this figure, it becomes clear that curvelet denoising does improve the inversion by stabilising the results. We notice that the higher the threshold the smoother is the estimated model. As discussed above, higher thresholds reduce amplitudes, which results in smaller impedance variations no longer being resolved. For both traces, the threshold of 7.5σ led to the best visual match (regarding how good contrasts were resolved) between estimated and real model.

For comparison, Figure 6 shows how increasing noise makes the inversion of the unfiltered data (trace 276) unstable by the presence of high-frequency oscillations. The inversion rms errors from lower to higher noise levels are 0.3204, 0.5909 and 0.9155, respectively.

Coloured noise. We next repeated the above experiments with coloured noise. All results from filtering and inversion considering coloured Gaussian noise with a frequency band limited to those of the data) are summarised in Table 2.

	Threshold (x σ)	**PSNR**		**Error**
		value(dB)	**change**	
Noise		**10e-3**		
	5	29.7505	+1.2513	0.1410
	7.5	30.0321	+1.6092	0.1336
	10	29.9384	+1.4586	0.0743
	12	29.5055	+1.0189	0.0518
Noise		**20e-3**		
	5	24.5904	+2.1109	0.2404
	7.5	25.6695	+3.2545	0.1415
	10	26.2300	+3.7880	0.0992
	12	26.1217	+3.6956	0.0693
Noise		**30e-3**		
	5	21.3389	+2.4640	0.3706
	7.5	24.0440	+4.1460	0.2810
	10	24.0923	+5.1772	0.1223
	12	24.2875	+5.3757	0.1332

Table 2: Results from coloured (band-limited white) noise tests in the Marmousi section.

Wile the general behaviour is similar to the previous case, we see that curvelet filtering has more difficulties with coloured noise. We note a lower PSNR and higher rms error than for white noise.

Figure 7 shows the results of filtering with a threshold of 10σ at three noise levels. It is clear from this figure that the noise can not be satisfactorily removed to guarantee a good visual quality even though relevant reflections can still be distinguished from noise. Moreover, small reflections are hardly recovered and close events (peaks and/or troughs in data) can not be resolved, in the worst case scenario being reconstructed as a single one.

Results from inversion at a noise level of $\sigma = 20$e-3 are shown in Figure 8. We notice that denoising improves the inversion results. Threshold values of about 10 to 12σ give the best results, even though both have, in general, lower values than the real model, resulting from a lack of low frequencies, i.e., the low-frequency part of the spectrum is most affected by the denoising procedure.

Real data - Marimbá data set

White Gaussian noise. Usually, poststack data have already been processed through many steps and corrections. Therefore, high noise levels can rarely be found. Nevertheless, we considered a noise level of $\sigma = 50$e-3 to be the worst case for the real-data example and tested this value in addition to the three levels used in the synthetic tests. For the denoising tests on real data, we used statistical and deterministic wavelet estimation. A summary of the results with white noise is presented in Table 3. Most of the observations of the synthetic analysis remain valid here, though only for higher noise levels and larger thresholds.

Figure 9 shows the filtering results for four noise levels considering a threshold of 10σ. Like for the synthetic data, the shallower part is stronger affected for increasing noise and threshold values. Furthermore, the zooms of traces 56 and 156 show that denoising can fairly approximate the true amplitude values. The denoised and real traces can hardly be distinguished from each other, even though very close reflections can not be distinguished, being treated as a single event.

Faults are important geological structures for reservoir discoveries, controlling oil migration and thus accumulation. For the present dataset, they appear mostly in the shallower part and with small lengths and widths. After denoising, most of them disappear depending on the threshold values. A possible simplistic solution to this would be the previously mentioned directional control, ensuring that most curvelets associated with the main fault dips are kept. Despite these shortcomings, denoising did provide visually consistent seismic sections for interpretation purposes.

The real-data inversion results also follow the synthetic ones. Figures 10 and 11 show the results without denoising for a statistical and a deterministic wavelet as input to inversion, respectively. We immediately

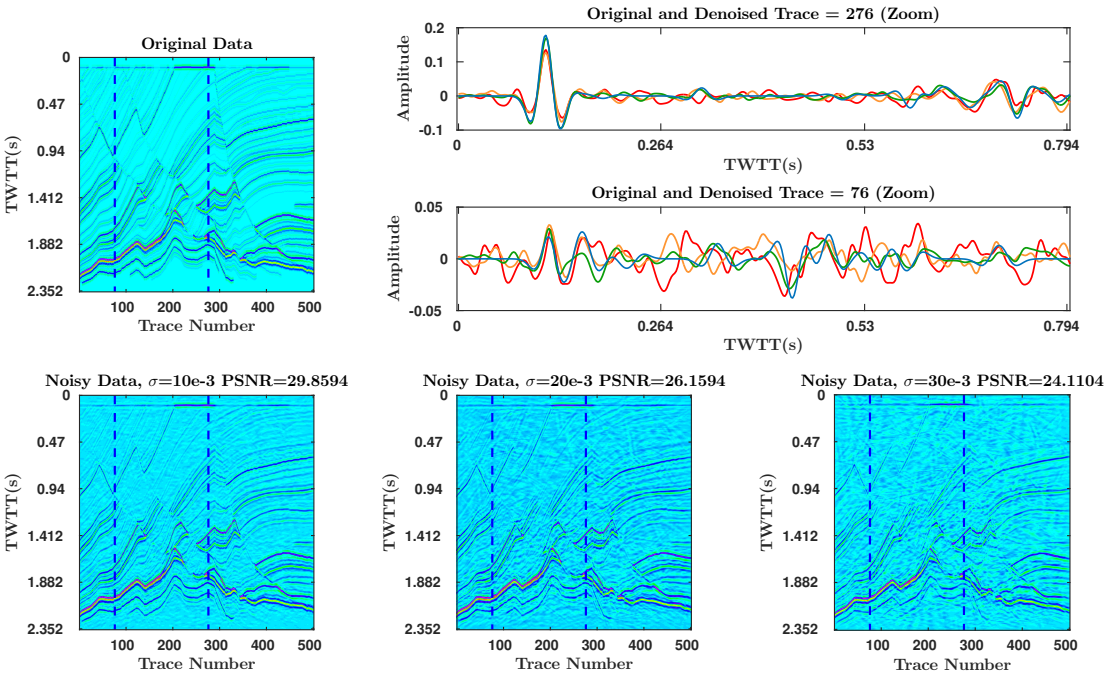

Figure 7: Denoising results at three noise levels and a threshold of 10 times the noise level. In graphs, blue is the original trace and red, orange and green correspond to noise from higher to lower level, respectively.

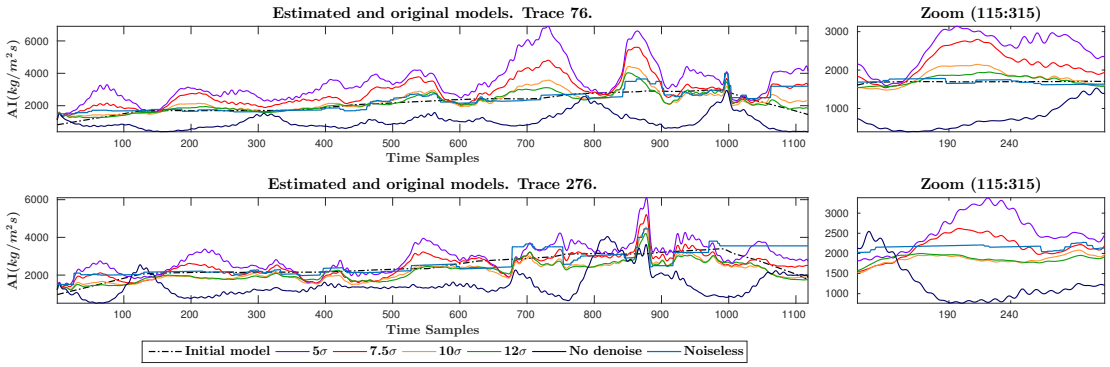

Figure 8: Inversion results for traces 76 and 276 after curvelet filtering the image polluted with coloured Gaussian noise of $\sigma = 20\text{e-}3$. All thresholds are shown.

notice that the shallower and deeper parts are more affected because they have smaller absolute amplitudes values. Also, we observe that the inversion reconstructs the high-frequency information associated with noise. This effect could be reduced by changing the noise parameter in the inversion. However, studying the performance of the inversion algorithm is not the focus of this work. For this reason, we kept this parameter untouched in order to truly study the effects of denoising. Finally, we observe that the results using the deterministic wavelet are more stable than those using the statistical one, being even more stable than the HR-inversion results, despite the considerable mismatch in the shallower part.

Figures 12 and 13 show the real-data inversion results after denoising for a noise level of 30e-3 with the statistical and deterministic wavelets, respectively. Results for the latter do not change much with the threshold value. However, for the former, the estimates show more stability. The observed lack of lower

	Threshold (x σ)	PSNR value(dB)	PSNR change	Error Stat.	Error Deter.
Noise		**10e-3**			
	5	39.0469	-0.9663	0.0529	0.4095
	7.5	37.5096	-2.5036	0.0472	0.3951
	10	36.0374	-3.9758	0.0547	0.3809
	12	35.0627	-4.9505	0.0515	0.3752
Noise		**20e-3**			
	5	35.8425	+1.8537	0.0641	0.3718
	7.5	33.7241	-0.2290	0.0548	0.3345
	10	32.1791	-1.7740	0.0472	0.3079
	12	31.1805	-2.7726	0.0423	0.2789
Noise		**30e-3**			
	5	33.6075	+3.1245	0.0524	0.3552
	7.5	31.5037	+1.0206	0.0447	0.3007
	10	29.8668	-0.6163	0.0395	0.2562
	12	28.8384	-1.6447	0.0342	0.2291
Noise		**50e-3**			
	5	30.7251	+4.6974	0.0510	0.2989
	7.5	28.5112	+2.4835	0.0397	0.2331
	10	26.8586	+0.8309	0.0249	0.1757
	12	25.8467	-0.1810	0.0225	0.1669

Table 3: Results from filtering white Gaussian noise from real data and the error in inversion for trace 156 from inline 69. Stat. and Deter. refer to whether the wavelet used in inversion is, respectively, statistical or deterministic.

frequencies that can easily be corrected by Fourier domain addition of the low-frequency model. Results are even more stable than those of HR inversion. This demonstrates the potential of conditioning the data before inversion using curvelet denoising in the presence of white Gaussian noise.

Coloured noise analysis. In the last test, we applied curvelet denoising to the real data with band-limited (coloured) Gaussian noise. A summary of the results is shown in Table 4, which exhibits the same characteristics (i.e., decreasing PSNR and rms errors with increasing thresholds values and noise levels) as before.

Figure 14 depicts the denoising results for four different levels of coloured noise. The general behaviour is the same as in the previous examples. However, in this case the sections show a significant amount of residual noise corrupting the data, which severely damages the shallower part with smaller amplitude reflections. The linear artifacts discussed previously are visually prominent in the region near trace 175 and depth 3.012 s. The zooms of traces 56 and 156 show again smoothing leading to smaller amplitude values and suppression of closely spaced reflections, particularly in the earlier part of the traces. However, in the second half of the traces, we actually observe an increase in resolution leading to a clearer distinction of close events and a gain in the amplitude of certain events. A possible explanation is residual noise in the original data that has been removed by the process together with the artificially added noise.

The inversion results using the filtered data for a noise level of 30e-3, again considering a statistical and a deterministic wavelet, are shown in Figures 15 and 16, respectively. As before, for the deterministic wavelet, results do not vary much from each other, though variation is bigger than in the white-noise case. Like there, inversion with a statistical wavelet allows for a better analysis of the denoising influence on the inversion, showing how the estimated models are more stable even when lacking low-frequency information. In response to the previously cited gain in amplitudes and clearer distinction of close events in the denoised traces, higher thresholding values provided a better match of the estimated to the reference model.

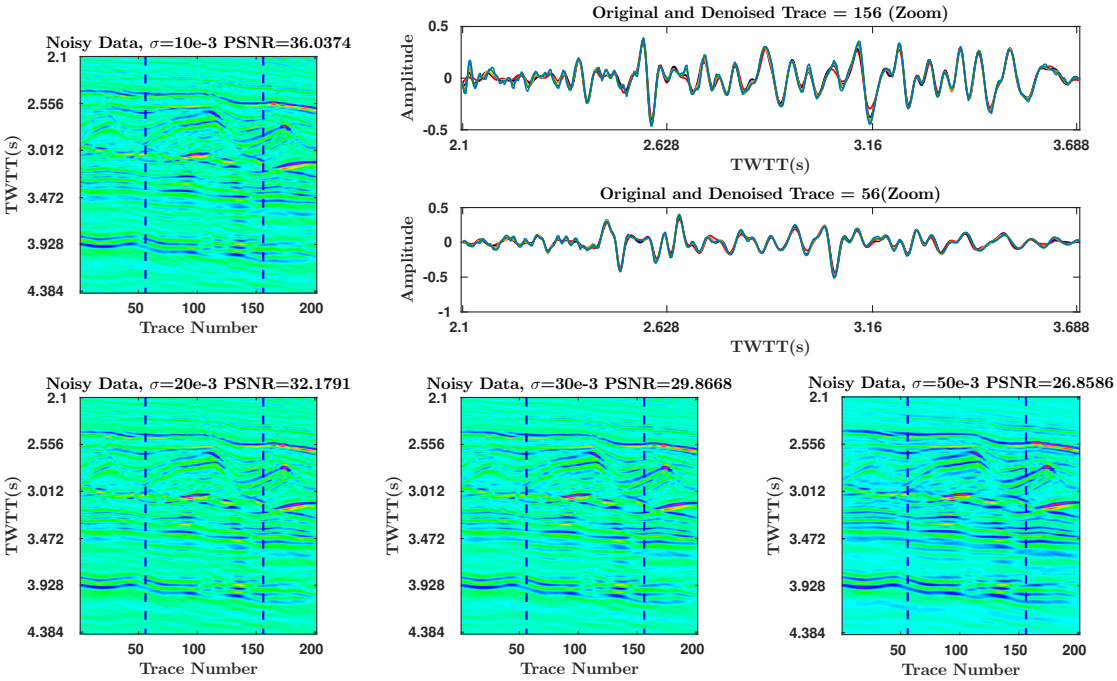

Figure 9: Denoising results considering four Gaussian white noise levels and a threshold of 10 times the noise level. In the graphs, blue is the original trace and red, dark blue, orange and green correspond to noise from higher to lower level, respectively.

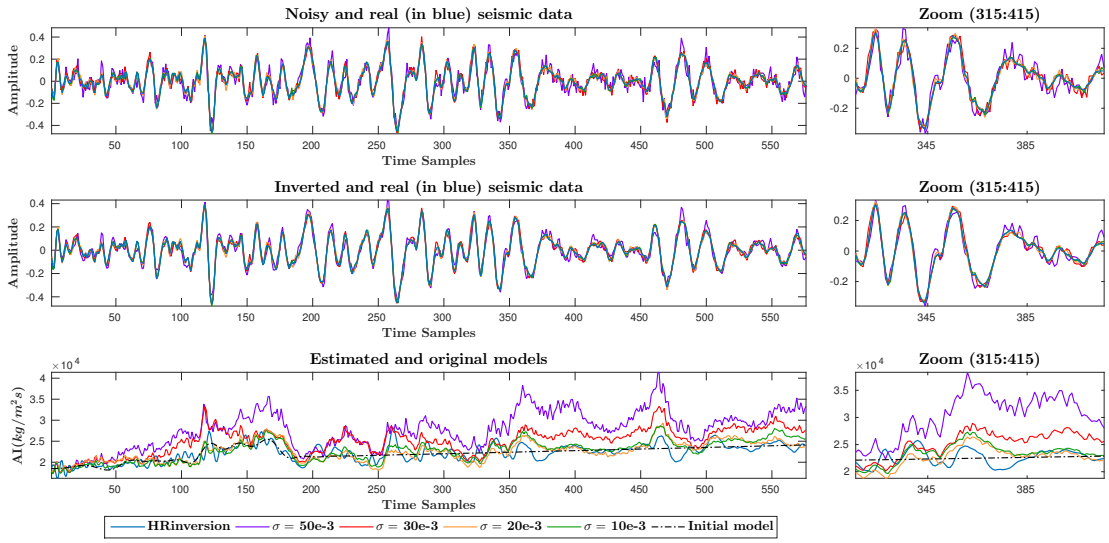

Figure 10: Inversion of trace 156 using a statistical wavelet from real seismic section without curvelet filtering, considering σ = 10e-3 (green), 20e-3 (yellow), 30e-3 (red) and 50e-3 (purple) white Gaussian noises.

CONCLUSION

In this work, we have investigated the benefits of curvelet denoising as a preconditioning method to acoustic inversion of poststack seismic data. Our objective was to evaluate if the curvelet denoising is able to

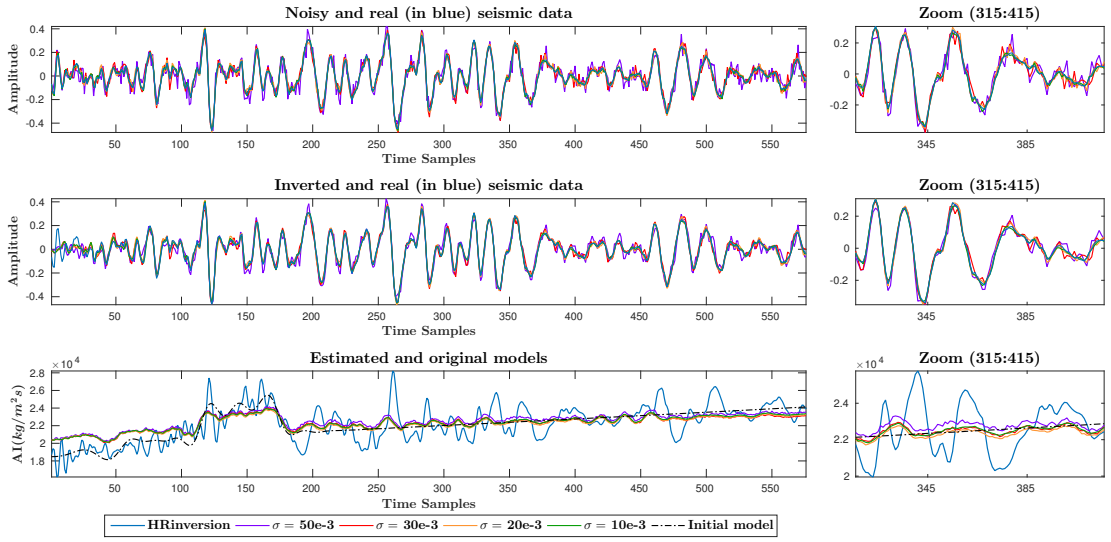

Figure 11: Inversion of trace 156 using a deterministic wavelet from real seismic section without curvelet filtering, considering σ = 10e-3 (green), 20e-3 (yellow), 30e-3 (red) and 50e-3 (purple) white Gaussian noises.

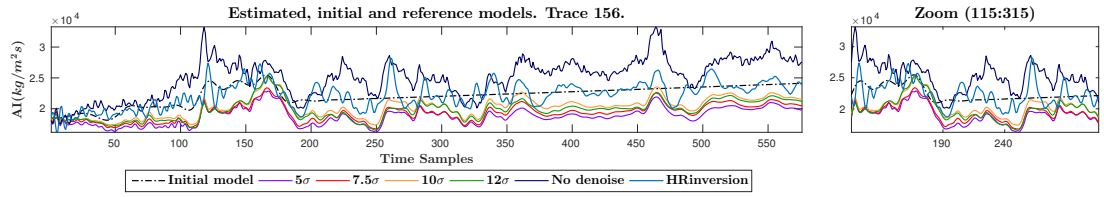

Figure 12: Inversion results using a statistical wavelet for trace 156 from inline 69 after curvelet filtering the image corrupted with white Gaussian noise of σ = 30e-3. All thresholds are shown.

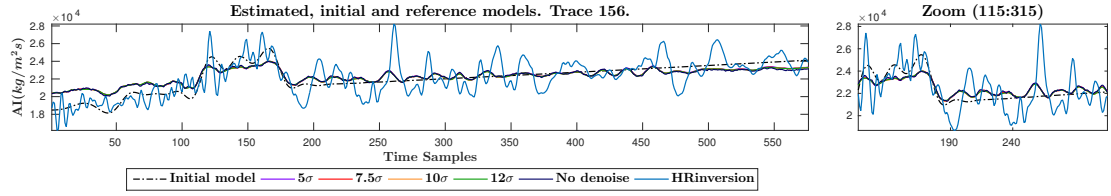

Figure 13: Inversion results using a deterministic wavelet for trace 156 from inline 69 after curvelet filtering the image corrupted with white Gaussian noise of σ = 30e-3. All thresholds are shown.

increase the resolution without degrading the signal-to-noise ratio (SNR). For this purpose, two data sets were contaminated with white and coloured noise for different SNRs, from a rather low one to a highest value that is uncommon in a pre-processed seismic data.

The tests were performed on synthetic and real data. We used the synthetic data set from the Marmousi model and a real data set from the Marimba oil field in the Campos Basin, offshore Brazil. All tests led to similar conclusions. The investigated curvelet-denoising methodology clearly increased the SNR. The quality of the outcome strongly depends on the choice of the coefficients.

Because our filtering is based on a global threshold assumption, the variation in the wavelength with

	Threshold (x σ)	PSNR value(dB)	PSNR change	Error Stat.	Error Deter.
Noise		**10e-3**			
	5	36.2819	-1.8455	0.1155	0.41
	7.5	35.6073	-2.5202	0.0637	0.3967
	10	34.7581	-3.3694	0.0743	0.4062
	12	34.1255	-4.0019	0.0623	0.3720
Noise		**20e-3**			
	5	31.8366	-0.2867	0.08	0.3475
	7.5	31.3997	-0.7236	0.0896	0.3394
	10	30.6969	-1.4265	0.0664	0.3599
	12	30.1840	-1.9393	0.0697	0.3062
Noise		**30e-3**			
	5	28.9805	+0.4505	0.1465	0.3548
	7.5	28.8157	+0.2858	0.1115	0.2566
	10	28.4109	-0.1191	0.0877	0.2639
	12	27.8585	-0.6715	0.0951	0.2370
Noise		**50e-3**			
	5	25.5412	+1.4334	0.2236	0.3247
	7.5	25.6641	+1.5563	0.2598	0.1915
	10	25.5789	+1.4711	0.1042	0.1181
	12	25.1404	+1.0325	0.1754	0.1905

Table 4: Results from filtering band-limited white Gaussian noise from real data and the error in inversion for trace 156 from inline 69. Stat. and Deter. refer to whether the wavelet used in inversion is, respectively, statistical or deterministic.

depth is not considered. The decreasing of the SNR for shallower reflections is a consequence of the application of a hard threshold value, motivated by the attempt to achieve improvements in deeper parts.

Future investigations will have to find alternative strategies of filtering that are capable of reducing the noise of the coefficients in an efficient manner so that coefficients associated with events of lower energy are not filtered with the same threshold as coefficients of higher energy. Furthermore, the investigated methodology provided encouraging results to justify evaluating its performance in the context of prestack inversion of seismic data, e.g., for amplitude variation with offset and full-waveform inversion.

ACKNOWLEDGEMENTS

This research was supported by the Brazilian research agencies CAPES, CNPq, FAPESP and FINEP. The first author V. M. Gomes thanks the GISIS (Grupo de Imageamento Sísmico e Inversão Sísmica) for allowing the use of its laboratories during the tests. H. B. Santos is grateful to Petrobras, ANP and PRH-PB230 for his fellowships. H. B. Santos, J. Schleicher, and A. Novais thank CNPq for the financial support by the INCT-GP (Instituto Nacional de Ciências e Tecnologia em Geofísica do Petróleo). Additional support for the authors was provided by the sponsors of the *Wave Inversion Technology (WIT) Consortium*, Germany.

REFERENCES

Abma, R. and Claerbout, J. (1995). Lateral prediction for noise attenuation by t-x and f-x techniques. *Geophysics*, 60(6):1887–1896.

Candès, E., Demanet, L., Donoho, D., and Ying, L. (2006). Fast discrete curvelet transforms. *Multiscale Modeling & Simulation*, 5(3):861–899.

Candès, E. J. and Donoho, D. L. (2000). Curvelets: A surprisingly effective nonadaptive representation for objects with edges. Technical Report No. 28, Stanford University.

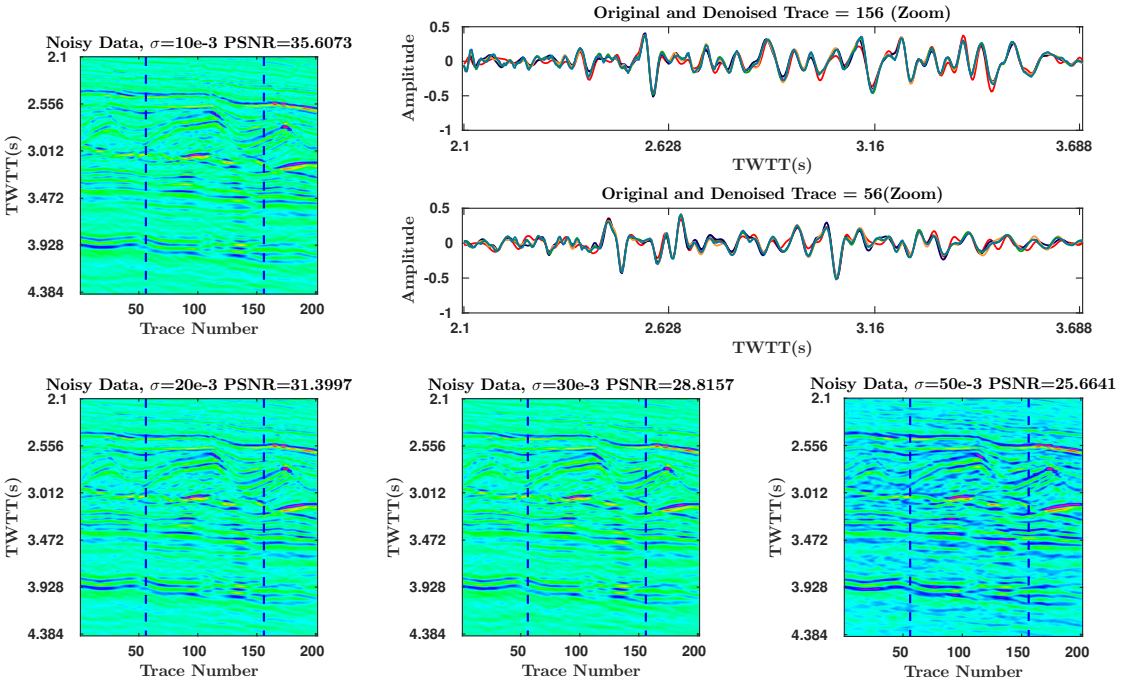

Figure 14: Denoising results considering four band-limited (coloured) Gaussian noise levels and a threshold of 7.5 times the noise level. In the graphs, blue is the original trace and red, dark blue, orange and green correspond to noise from higher to lower level, respectively.

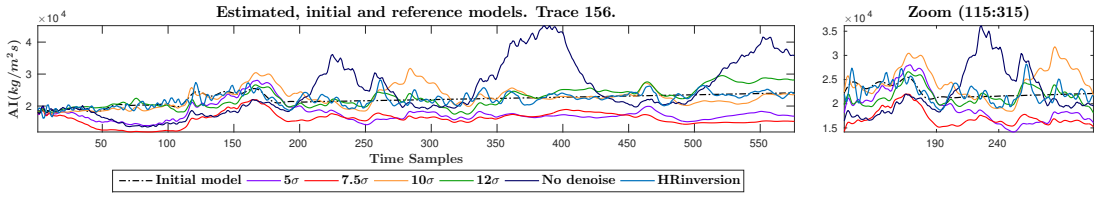

Figure 15: Inversion results using a statistical wavelet for trace 156 from inline 69 after curvelet filtering the image corrupted with band-limited Gaussian white noise of σ = 30e-3. All thresholds are shown.

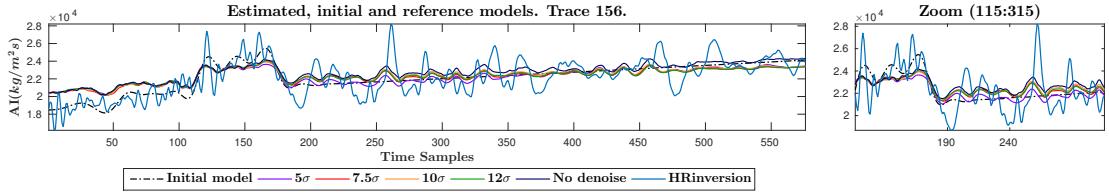

Figure 16: Inversion results using a deterministic wavelet for trace 156 from inline 69 after curvelet filtering the image corrupted with band-limited (coloured) Gaussian noise of σ = 30e-3. All thresholds are shown.

Candès, E. J. and Donoho, D. L. (2003). New tight frames of curvelets and optimal representations of objects with piecewise C^2 singularities. *Communications on Pure and Applied Mathematics*, 57(2):219–266.

Chauris, H. and Nguyen, T. (2008). Seismic demigration/migration in the curvelet domain. *Geophysics*, 73(2):S35–S46.

de Macedo, I. A., da Silva, C. B., de Figueiredo, J., and Omoboya, B. (2017). Comparison between deterministic and statistical wavelet estimation methods through predictive deconvolution: Seismic to well tie example from the North Sea. *Journal of Applied Geophysics*, 136:298–314.

Górszczyk, A., Adamczyk, A., and Malinowski, M. (2014). Application of curvelet denoising to 2D and 3D seismic data — practical considerations. *Journal of Applied Geophysics*, 105:78–94.

Hennenfent, G., Fenelon, L., and Herrmann, F. J. (2010). Nonequispaced curvelet transform for seismic data reconstruction: A sparsity-promoting approach. *Geophysics*, 75(6):WB203–WB210.

Hennenfent, G. and Herrmann, F. (2006). Seismic denoising with nonuniformly sampled curvelets. *Computing in Science & Engineering*, 8(3):16–25.

Herrmann, F. J. and Hennenfent, G. (2008). Non-parametric seismic data recovery with curvelet frames. *Geophysical Journal International*, 173(1):233–248.

Ma, J. and Plonka, G. (2010). The curvelet transform. *IEEE Signal Processing Magazine*, 27(2):118–133.

Mallat, S. (1999). *A Wavelet Tour of Signal Processing, Second Edition (Wavelet Analysis & Its Applications)*. Academic Press.

McMechan, G. A. (1983). p-x imaging by localized slant stacks of t-x data. *Geophysical Journal International*, 72(1):213–221.

Neelamani, R., Baumstein, A. I., Gillard, D. G., Hadidi, M. T., and Soroka, W. L. (2008). Coherent and random noise attenuation using the curvelet transform. *The Leading Edge*, 27(2):240–248.

Parolai, S. (2009). Denoising of seismograms using the S transform. *Bulletin of the Seismological Society of America*, 99(1):226–234.

Robinson, E. A. (1954). *Predictive decomposition of time series with applications to seismic exploration*. PhD thesis, Massachusetts Institute of Technology.

Shan, H., Ma, J., and Yang, H. (2009). Comparisons of wavelets, contourlets and curvelets in seismic denoising. *Journal of Applied Geophysics*, 69(2):103–115.

Starck, J.-L., Candès, E. J., and Donoho, D. L. (2002). The curvelet transform for image denoising. *IEEE Transactions on image processing*, 11(6):670–684.

Ulrych, T. J. and Sacchi, M. D. (2005). *Information-based inversion and processing with applications*, volume 36. Elsevier.

Versteeg, R. (1994). The marmousi experience: Velocity model determination on a synthetic complex data set. *The Leading Edge*, 13(9):927–936.

Wang, D.-L., Tong, Z.-F., Tang, C., and Zhu, H. (2010). An iterative curvelet thresholding algorithm for seismic random noise attenuation. *Applied Geophysics*, 7(4):315–324.

Yuan, S., Wang, S., Luo, C., and He, Y. (2015). Simultaneous multitrace impedance inversion with transform-domain sparsity promotion. *Geophysics*, 80(2):R71–R80.